Dual-Defect Manipulation Enables Efficient and Spectrally Stable Blue Perovskite Light-Emitting Diodes

Chengxi Zhang, Hao Yuan, Lingmei Kong, Lin Wang, Yuanzhi Wang, Yunguo Li, Yingguo Yang, Lyudmila Turyanska,* and Xuyong Yang*

Performance of blue solution-processed perovskite light-emitting diodes (LEDs) is limited by availability of blue perovskite materials. Herein, 4-(trifluoromethyl)benzoyl ammonium bromide (4-TMBABr) is used with abundant N–H and C=O groups to passivate the defects and produce highly stable $PEA_xPA_{2-x}(CsPbBr_3)_{n-1}PbBr_4$ perovskites for blue LED applications. The N–H group in the 4-TMBABr suppresses the Br-ion mismatch through hydrogen bonds (N-H···Br) and C=O group coordinates the unsaturated lead dangling bonds (C=O:Pb). The effective defect passivation by 4-TMBABr reduces the nonradiative recombination in the perovskite films, hence enhancing its optical performance. In the LED structure, the sodium bis(trifluoromethanesulfonyl)imide (SBTI) modified NiO_x films are used to improve the hole transport and to inhibit the fluorescence quenching of the perovskite layer. The dual-defect manipulation strategy is advantageous for producing efficient and spectrally stable blue perovskite LEDs, and the authors demonstrate an LED with maximum luminance of 1094 cd m^{-2} and external quantum efficiency of 10.3%. This work can inform and underpin future development of blue perovskite LEDs with highly efficient and stable performance.

1. Introduction

Metal halide perovskite materials have emerged as promising candidates for optoelectronic applications,[1–3] particularly for light-emitting diodes (LEDs). Since the first realization of perovskite LED (PeLED) in 2014 with an external quantum efficiency (EQE) of ≈0.1%,[4] the device performance was greatly improved for green, red and near-infrared PeLEDs (EQE over 20%).[5–8] This was enabled by advancements in the metal halide perovskite synthesis and by fundamental understanding of the physics of interfaces between perovskite luminescent layer and electron/hole-transport layers.[5,8–12] However, the performance of blue PeLEDs remains much lower than that of other-colour PeLEDs.[12,13] Recently, quasi-2D perovskites with quantum confinement and dielectric confinement have shown great prospects for blue light emission. The film formation process of quasi-2D perovskite from precursor to a solid film mainly consists of two steps: nucleation and growth. Generally, rapid nucleation and slow crystal growth are effective methods to obtain high-quality films. However, in the complex multi-cation perovskite precursor system, defects are inevitably formed during the crystallization of quasi-2D perovskite films due to the non-homogeneous nucleation and uncontrollable growth.[14] These defects cause trapping of injection carriers, resulting in increased nonradiative recombination and lower luminous efficiency of the device. Although passivation agents, including organic molecules (diphenylphosphinic chloride),[15] organic ammonium[16] and halide salts (2-phenylethanamine bromide, guanidinium bromide, yttrium (III) chloride),[17–20] inorganic passivators (potassium salt)[21] are currently used to passivate defects (halide

C. Zhang, H. Yuan, L. Kong, L. Wang, Y. Wang, X. Yang
Key Laboratory of Advanced Display and System Applications of Ministry of Education
Shanghai University
149 Yanchang Road, Shanghai 200072, P. R. China
E-mail: yangxy@shu.edu.cn

Y. Li
CAS Key Laboratory of Crust-Mantle Materials and Environments
School of Earth and Space Sciences
University of Science and Technology of China
Hefei 230026, P. R. China

Y. Yang
Shanghai Synchrotron Radiation Facility (SSRF)
Zhangjiang Lab
Shanghai Advanced Research Institute
Chinese Academy of Sciences
Shanghai 201204, P. R. China

L. Turyanska
Faculty of Engineering
University of Nottingham
Nottingham NG7 2RD, UK
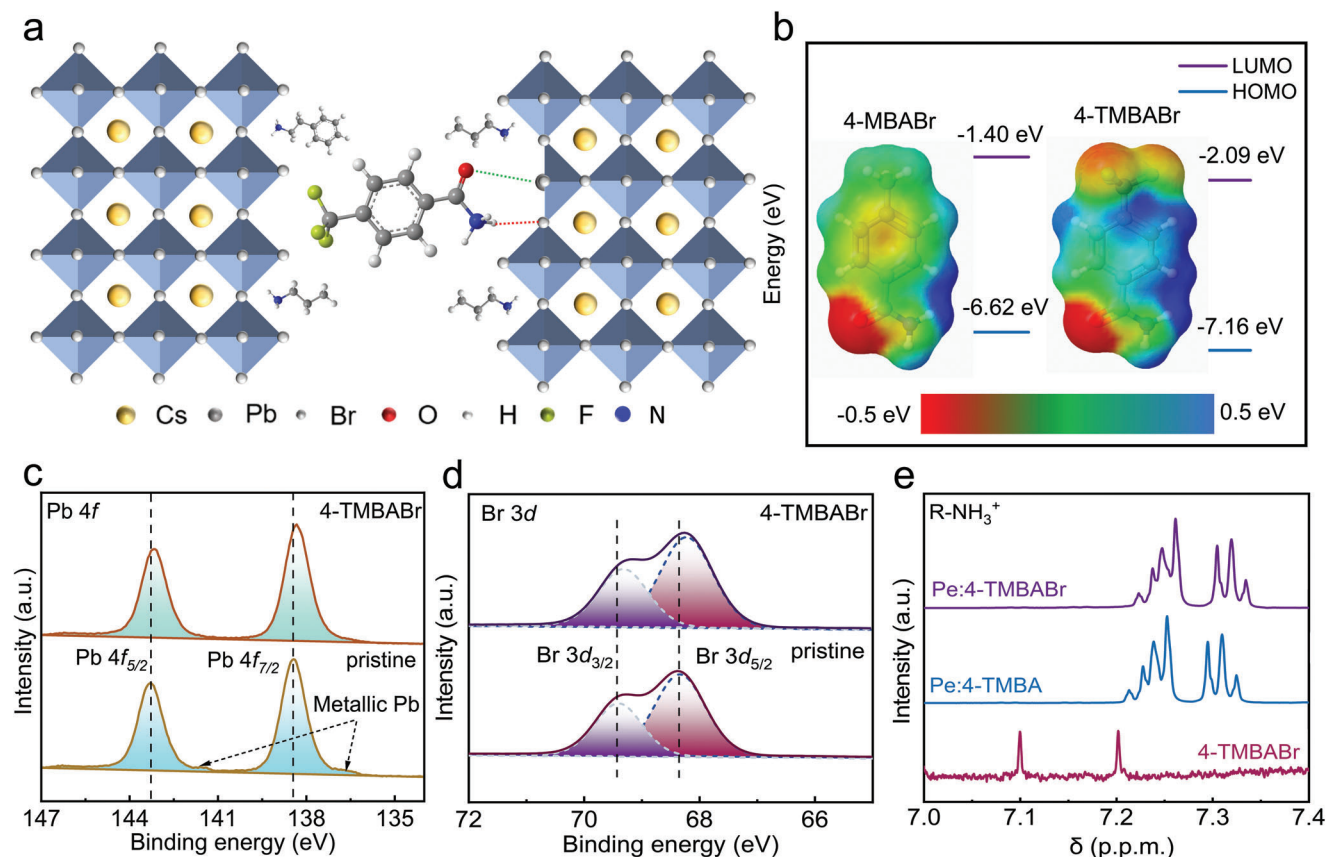E-mail: lyudmila.turyanska@nottingham.ac.uk

Figure 1. a) Schematic illustration of defect passivation of the perovskite grain boundaries by 4-TMBABr. b) Simulated ground-state geometries and electrostatic potentials (ESP) of 4-TMBABr anion and 4-MBA anion without F replacement. High-resolution XPS spectra of pristine and 4-TMBABrB treated perovskite films for c) Pb 4f and d) Br 3d. e) ^{1}H nuclear magnetic resonance (NMR) spectra of 4-TMBABr, perovskite: 4-TMBA, and perovskite: 4-TMBABr in deuterated dimethylsulfoxide-d6 (DMSO-d6) solution.

vacancies and Pb^{2+} defects) on quasi-2D blue perovskite surfaces and at grain boundaries by chemical coordination, there is still a need for more effective strategies to achieve high performance of blue PeLEDs.

Carrier (hole and electron) transport/injection layers are optimized to reduce carrier injection barrier hence improving the performance of blue PeLEDs.[22–24] NiO_x is widely used as an efficient hole transport layer (HTL) in perovskite optoelectronic devices, as it provides optimal energy band alignment for hole transport. However, the direct contact between the NiO_x film and the perovskite film not only causes fluorescence quenching of the perovskite film, but also affects the crystallinity and stability of the perovskite films.[25,26] In addition, the energy level mismatch between the NiO_x and perovskite layers can adversely impact on the radiation recombination rate and device performance.[21] Therefore, optimizing the properties of the interface between the NiO_x and perovskite films to enhance the hole injection capability is an effective way to improve the device performance.

In this work, we developed a synergetic approach to produce high-efficiency blue-emitting PeLED, which combines the defect passivation strategy to regulate the growth of quasi-2D perovskite films with improved modified NiO_x HTL interface. To grow high quality low defect perovskite films, we introduce a passivator, 4-(trifluoromethyl) benzoyl ammonium bro-

mide (4-TMBABr), to suppress the Br-ion mismatch through hydrogen bonds (N—H··Br) and to coordinate the unsaturated lead dangling bonds (C=O:Pb). The deposition of sodium bis(trifluoromethanesulfonyl) imide (SBTI) onto the surface of NiO_x improves the quality of the interface and reduces the energy barrier for hole injection, while reducing the density of defects on the NiO_x surface and suppressing the nonradiative recombination. Reduced defect density in the perovskite layer and at the interface, combined with improved charge transport is favorable for LED performance, and allows us to demonstrate an efficient and stable blue PeLEDs with a peak EQE over 10% and a prolong maximum operational lifetime of 52.3 min.

2. Results and Discussion

Surface defects in perovskite crystals mainly include halide defects (negatively charged halide dangling bonds) and Pb^{2+} defects.[27] The dual passivation additive, 4-TMBABr, can form strong hydrogen bonds with halide ions due to the electron withdrawing F atom (**Figure 1**a), which can suppress the formation of halide dangling bonds. Moreover, the lone pair of electrons in 4-TMBABr molecules can be coordinated with the mismatched lead ion to passivate the Pb^{2+} defects. The density functional theory (DFT) calculation revealed that the formation energy of

**ADVANCED
SCIENCE NEWS**

www.advancedsciencenews.com

**ADVANCED
OPTICAL
MATERIALS**

www.advopticalmat.de

dangling Pb^{2+} was increased from 1.51 to 3.97 eV following interaction of the surface Pb^{2+} with fluorine from 4-TMBA, while the formation energy is 6.7 eV for the perovskites with C=O adsorbed on the surface. These results demonstrate that the Pb^{2+} defect formation is more effectively suppressed by C=O functional group compared with F functional groups of 4-TMBABr molecule. The ground-state geometries and electrostatic potentials (ESP) simulations of 4-TMBABr and 4-methylbenzamide (4-MBA) anions without F replacement revealed a decreased charge density in the C=O group when the methyl group attached to the benzene ring is fluorinated, which leads to a softer C=O bonding and consequently a stronger interaction with surface Pb^{2+} (Figure 1b). Therefore, the perovskite structures with large number of dangling bonds at the grain boundaries are effectively passivated due to the formed bonds between the neighboring surfaces (4-TMBABr molecule).

X-ray photoelectron spectroscopy (XPS) measurements were performed to examine the interaction of 4-TMBABr with lead and halide defects. The characteristic binding energy peaks for Pb $4f$ and Br $3d$ shift by 0.2 eV toward low-energy for the 4-TMBABr-modified perovskite film compared to those for the pristine perovskite film (Figure 1c,d). This indicates that the cationic charge on the Pb ion decreases as a result of the interaction with C=O, which donates the lone electron pair to the empty $6p$ orbital of Pb^{2+}.[28] The shift toward lower binding energy for Br $3d$ peak is caused by the disturbance due to the electron donation from 4-TMBABr to Pb^{2+} through the formation of Lewis adducts, which results in the change of static interactions between Pb^{2+} and Br^-. Moreover, the metallic Pb signals at 141.5 and 136.7 eV, observed for pristine perovskite film, are not found in 4-TMBABr perovskite film, which indicates that the formation of metallic Pb is also suppressed.[29] The N 1s resonance is shifted by 0.2 eV to higher binding energy with the incorporation of 4-TMBA$^+$ (Figure S1, Supporting Information), demonstrating a change of electron cloud distribution of N atom compared to the pristine perovskite film.

In order to gain deeper insights into the chemical interaction between 4-TMBABr and perovskites, we measured the nuclear magnetic resonance (NMR) spectroscopy for 4-TMBABr and perovskite: 4-TMBABr, which were dissolved in deuterated DMSO-d6 (Figure 1e). The peak ($\approx$ 7.20 ppm) of ^{1}H NMR from R-NH$_3^+$ in the pristine 4-TMBABr was shifted toward the low chemical shift (7.22 ppm) in the perovskite, indicating the coordination of bromine on perovskite with R-NH$_3^+$ in 4-TMBABr. The interaction between the 4-TMBABr and the PbBr$_6^{2-}$ framework was further confirmed by Fourier transform infrared (FTIR) spectroscopy studies, which revealed a shift of C=O stretching vibration peak from 1657 cm^{-1} for 4-TMBABr, to 1644 cm^{-1} for 4-TMBABr/PbBr$_2$ powder (Figure S2, Supporting Information). The energies of scissoring and stretching vibration of N-H also shift to lower values from 1580 and 3376 cm^{-1} for 4-TMBABr to 1578 and 3372 cm^{-1} for 4-TMBABr/PbBr$_2$, respectively, confirming hydrogen bonding interaction between the N−H and the perovskite. These results are in good agreement with the XPS results.

The effect of 4-TMBABr on the crystallization of the quasi-2D PEA$_x$PA$_{2-x}$(CsPbBr$_3$)$_{n-1}$PbBr$_4$ perovskite was probed with the X-ray diffraction (XRD) measurements (**Figure 2**a). The diffraction peaks observed at 14.6°and 29.3° are characteristics of (100) and

(200) planes of CsPbBr$_3$ perovskite, respectively.[30,31] The diffraction peaks observed at $2\theta < 13°$ belong to the low dimensional perovskites with $n = 2$ and $n = 1$ domains.[32] All characteristic peaks for perovskites were observed for all the samples, with no additional diffraction peaks appearing with increasing molar ratio of 4-TMBABr, which confirms that the 4-TMBABr is not incorporated into the perovskite lattice. The observed increase in diffraction peak intensity with increasing 4-TMBABr content suggests that 4-TMBABr promotes crystallization due to hydrogen bonding interactions with the PbBr$_6^{2-}$ framework leading to a decrease in crystal growth rate.[33] The grazing-incidence wide-angle X-ray scattering (GIWAXS) (Figure 2b; Figure S3, Supporting Information) and the UV–visible absorption (Figure 2c) measurements support this conclusion.

With increasing 4-TMBABr molar ratio, an enhanced PL intensity is observed for perovskite films, with PL quantum yields reaching a value of 57% for 5 mol% of 4-TMBABr (Figure 2d,f), and further increasing the 4-TMBABr concentration (7.5 mol%) results in the reduced optical properties of the perovskite film, likely due to the excess 4-TMBABr a affecting the crystallinity and phase distribution of perovskite films (Figure 2a,b). Time-resolved photoluminescence (TRPL) (Figure 2e; Table S1, Supporting Information) revealed an average decay time of 11.6 ns for 5% molar ratio of 4-TMBABr perovskite film, which is longer than that of pristine perovskite film (7.3 ns). The enhancement of PLQY and longer PL lifetime provides further evidence for effective defect passivation by 4-TMBABr and suppression of nonradiative recombination. It was found that the optical properties are improved with increasing 4-TMBABr molar ratio to 5%, after which no further improvement was achieved (Figure 2f). We envisage that this molar ratio is optimal for the defect density on the perovskite films.

The space-charge-limited current (SCLC) technique is employed to quantify the defect density (η_t) using the Equation (1):

$$\eta_t = \frac{2\epsilon_0\epsilon_r V_{TFL}}{ed^2} \qquad (1)$$

where ϵ_0, ϵ_r are the vacuum permittivity and relative permittivity, respectively, V_{TFL} is the intersection voltage of the trap-filled limit and ohmic regime (set in at $V_{TFL} = 1.59$ V for the pristine film, and 1.03 V for the 4-TMBABr modified film) (Figure S4, Supporting Information), e is the elemental charge and d is the thickness of perovskite films. The ϵ_r value of perovskite film is calculated from the measurements of perovskite film capacitance, C, (Figure S5, Supporting Information) using the following Equation (2):

$$C = \frac{\epsilon_0\epsilon_r S}{d} \qquad (2)$$

where S is the device area (4 mm^2). We estimate the trap state density $\eta_t = 3.42 \times 10^{17}$ cm^{-3} for 4-TMBABr treatment film, which is lower than that of pristine film ($\eta_t = 6.28 \times 10^{17}$ cm^{-3}), as expected due to 4-TMBABr defect passivation. The hysteresis of the electrical properties of perovskite films is typically attributed to ion migration.[34] Our electrical measurements revealed no measurable hysteresis in 4-TMBABr PeLEDs (Figure S6, Supporting Information), further confirming that 4-TMBABr molecules successfully passivate the defect-trap states
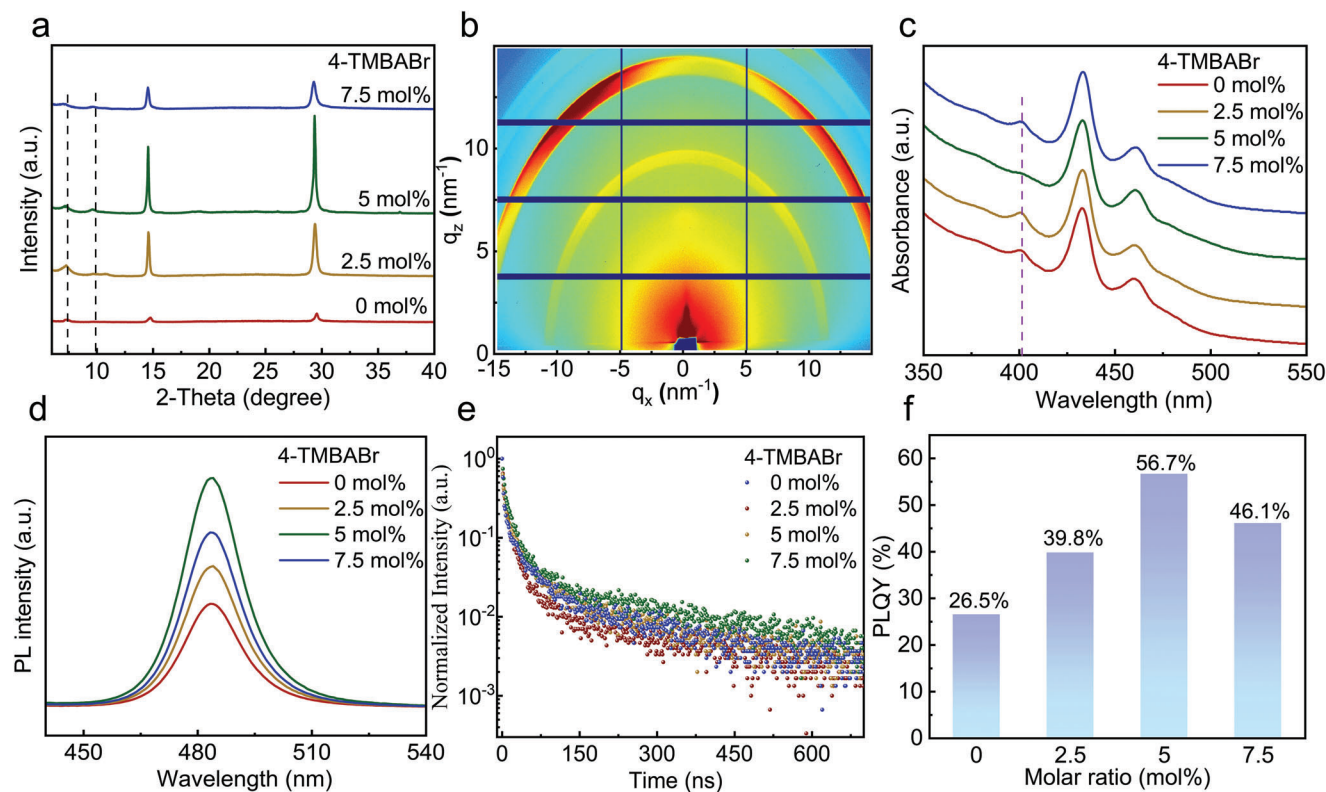
**ADVANCED
SCIENCE NEWS**

www.advancedsciencenews.com

**ADVANCED
OPTICAL
MATERIALS**

www.advopticalmat.de

Figure 2. a) X-ray diffraction (XRD) pattern of the quasi-2D perovskite produced with different molar ratio of 4-TMBABr. b) GIWAXS patterns of quasi-2D perovskite films prepared with 5% molar ratio of 4-TMBABr. Optical characterization of perovskites produced with different ratio of 4-TMBABr. c) UV–vis absorption spectra, d) PL spectra, e) time-resolved photoluminescence (TRPL), and f) photoluminescence quantum yield (PLQY) of perovskite films. The ITO/NiOx/SBTI/substrates were used to prepare the perovskite films.

and that ion migration through the grain boundaries has been suppressed.

NiO$_x$ exhibits a great potential as HTL to fabricate a stable PeLED due to their high carrier mobility, stable structural properties and better energy band matching with perovskite, however direct contact between the NiO$_x$ and perovskite easily cause PL quenching of perovskite film and can affect performance of perovskite film.[25,26] A multifunctional SBTI interface layer (the thickness < 2 nm) is used to eliminate these effects and to improve the surface properties of NiO$_x$ layer (**Figure 3**a; Figure S7, Supporting Information). The elemental maps of the NiO$_x$/SBTI films show homogeneous distribution of S, N, F, and Na, indicating that the SBTI is uniformly present on the NiO$_x$ film (Figure S8, Supporting Information). Atomic force microscopic (AFM) and scanning electron microscopic (SEM) images of the perovskite films deposited on NiO$_x$ film (Figure 3a–d) revealed presence of numerous pinholes with different sizes and shapes, and a surface roughness of 7.0 nm. In contrast, continuous perovskite films were formed in the presence of NiO$_x$/SBTI (Figure 3b,d) with noticeable improvement in grain size uniformity and significantly reduced surface roughness of 3.1 nm. This is mainly attributed to the existence of hydrophilic sulfate groups in the structure of SBTI, which improves the hydrophilicity of NiO$_x$/SBTI films and enhances the wetting ability of perovskite films, which is more conducive to the formation of perovskite films The measurements of the DMSO contact-angle on the NiO$_x$

films spin-coated with different concentrations of SBTI (Figure S9, Supporting Information) revealed a significant (≈3 times) decrease of the contact angle from 20.7° to 6.6° with increasing concentrations of SBTI from 0 to 5 mg mL^{-1}. Hence this treatment facilitates the formation of continuous perovskite films The device performance shows that the optimal SBTI concentration is 1 mg mL^{-1}, mainly because the thick SBTI modification layer will reduce the hole injection rate (Figure S10, Supporting Information), thus affecting the device performance. These results demonstrate the important roles of SBTI layer for preparation of high-quality perovskite films with reduced number of pinholes and low surface roughness.

Steady-state PL measurements were carried out to evaluate the influence of SBTI on the optical properties of perovskite films. The NiO$_x$/SBTI-deposited perovskite films have higher PL intensity compared to that for NiO$_x$ based perovskite films (Figure 3e), which is attributed to charge trapping on the defects and charge transfer at the NiO$_x$/perovskite interface. The PL lifetime of NiO$_x$/SBTI/perovskite is 8.94 ns, which is ≈2-times increase compared to that measured for of NiO$_x$/perovskite (4.36 ns) (Figure 3f). Importantly for LED applications, the optical transmittance (Figure S11, Supporting Information) of both the NiO$_x$ and NiO$_x$/SBTI films on quartz glass is unchanged, with the average transmittance of > 89% in the visible wavelength range from 400 to 800 nm, which means that the incorporation of SBTI will not affect light output of the device.
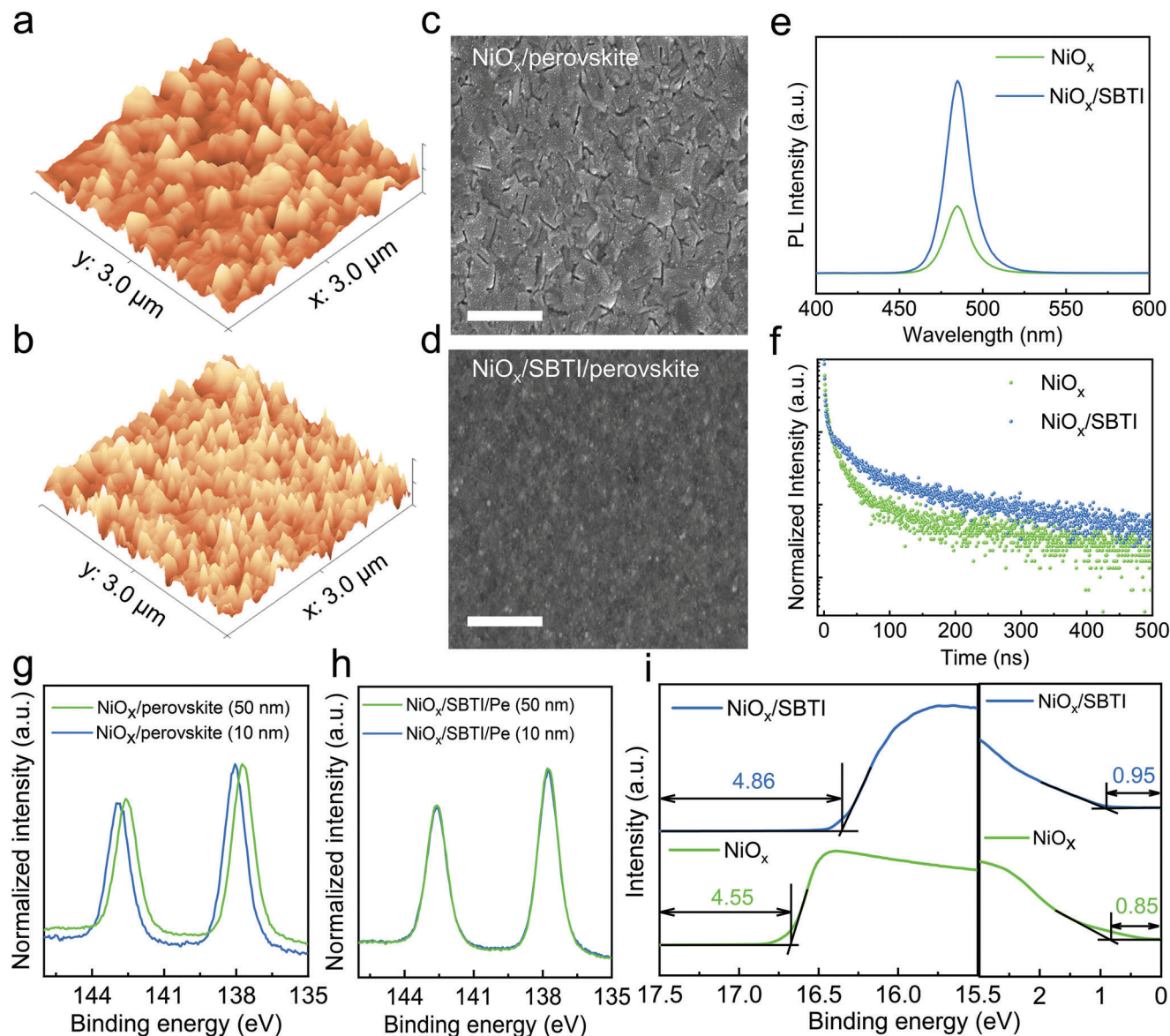
Figure 3. a,b) Representative atomic force microscopy topology maps and c,d) SEM images of 4-TMBABr based perovskite films based on NiO_x and NiO_x/SBTI, respectively. Room temperature photoluminescence spectra of perovskites on NiO_x and on NiO_x/SBTI. e) PL and f) TRPL. High-resolution Pb 4f XPS spectra of the perovskite film (10 nm and 50 nm thickness) deposited on g) ITO/NiO_x and h) ITO/NiO_x/SBTI substrates. i) UPS spectra of high binding energy secondary-electron cutoffs and valence-band edge regions of NiOx and NiO_x/SBTI films.

To further evaluate the effectiveness of the interface SBTI layer for promoting the crystallization of the perovskite film, the X-ray diffraction measurements were performed. We found that the XRD peak positions remained unchanged, indicating that the SBTI is not incorporated into the perovskite crystal lattice, and is accumulated at the grain-boundaries or at the interface between the layers. Moreover, the increased intensity of (100) and (200) peak confirmed enhanced crystallinity of perovskite film formed with the SBTI interface modification (Figure S12, Supporting Information), which is beneficial for enhanced optical properties and crystal stability.

To better understand the effect of SBTI on the perovskite crystal growth, perovskite films with different thicknesses were de-posited on the NiO_x and NiO_x/SBTI substrates. For perovskite films of different thicknesses (10 nm and 50 nm) deposited on NiO_x, an obvious shift of the Pb 4f peaks to a higher binding energy was observed, indicating an electron-deficient chemical state of the Pb atoms possibly due to the presence of halide vacancies (Figure 3g). In contrast, no measurable shift of Pb 4f binding energy was recorded for 10/50 nm-thick perovskite layer on NiO_x/SBTI (Figure 3h), demonstrating that the interface defects are effectively passivated by C=O groups of SBTI that act as Lewis bases for defect-healing by interacting with uncoordinated Pb^{2+}.[35] This chemical environment promotes similar crystal growth conditions at the interface as in the bulk films, thus leading to uniform grain size distribution. Furthermore, the
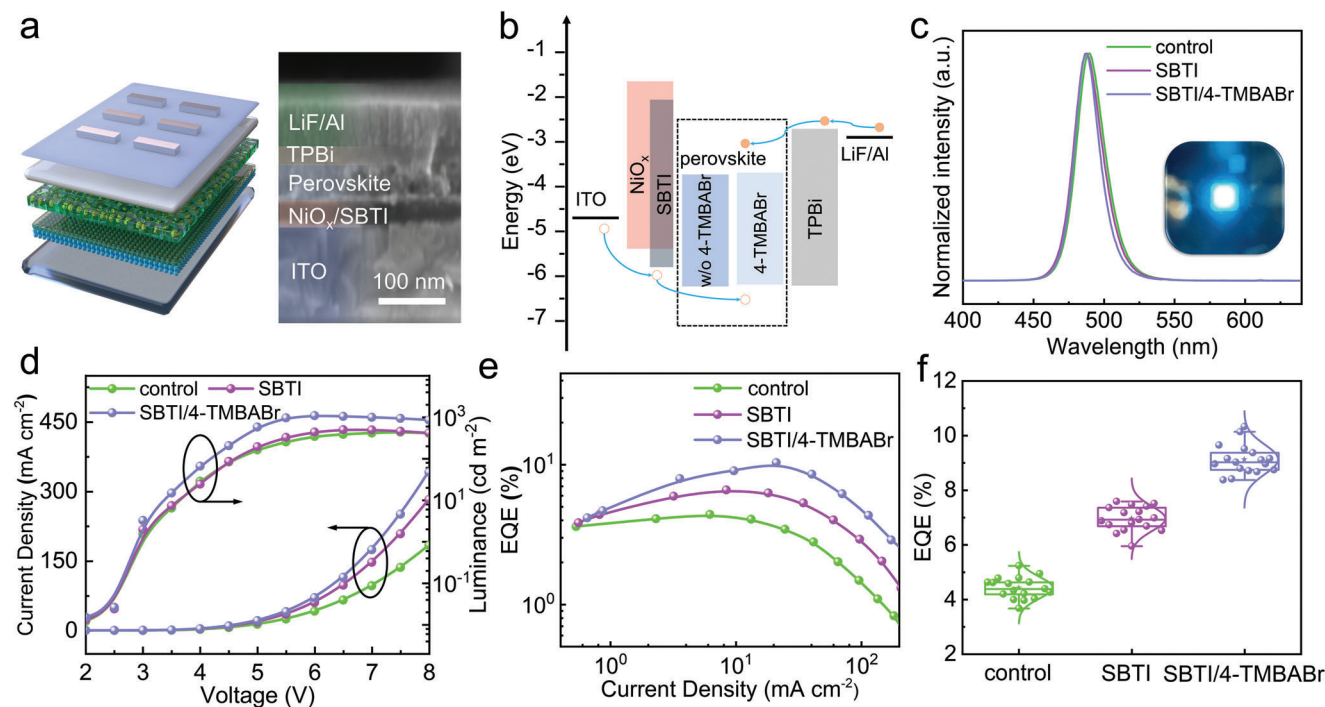
ADVANCED
SCIENCE NEWS
www.advancedsciencenews.com

ADVANCED
OPTICAL
MATERIALS
www.advopticalmat.de

Figure 4. a) Device structure and its corresponding cross-sectional SEM image of the blue PeLEDs with structure of glass/ITO/NiO_x/SBTI/Perovskite/TPBi/LiF/Al. b) Energy band diagram of the blue PeLEDs structure plotted using the results of UPS and optical measurements. c) EL spectra of NiOx, NiO_x/SBTI, and NiO_x/SBTI/4-TMBABr blue PeLEDs. The device structure and performance of PeLEDs Inset: Photograph of the device with bright blue emissions observed at V = 4 V. d) $J-L-V$ curves (Luminance is shown with subtracted background), e) EQE–J curves, f) statistical graph of blue PeLEDs.

improved interface properties between the perovskite and NiO_x with SBTI are advantageous to enhance the quality of perovskite films.

Effective carrier injection and charge balance are crucial to achieve high-performance PeLEDs. The XPS spectra of NiO_x and NiO_x/SBTI thin films exhibit three characteristic peaks at 853.8 eV, 855.3 eV, and 860.7 eV, corresponding to NiO, Ni_2O_3, and NiO_x.[36] The ratio of Ni^{3+}/Ni^{2+} in the NiO_x film is found to be 1.54, which is significantly lower than 2.27 for the NiO_x/SBTI film (Figure S13, Supporting Information). We ascribe this to the presence of free Na^+ in SBTI layer that are doped into the NiO lattice, the Na^+ entering the NiO lattice promote the increase of of Ni^{3+} concentration to maintain the charge neutrality. The Ni^{3+} state in NiO_x films generates p-type conductivity, which helps to improve the hole transport of the films (Figure S13, Supporting Information).[37,38]

Optical absorption spectra confirmed the band gap of 3.75 eV for both the NiO_x and NiO_x/SBTI films (Figure S14, Supporting Information).It was found that the introduction of the interfacial SBTI layer increases the work function from 4.55 eV for NiO_x to 4.86 eV for NiO_x/SBTI due to the formation of molecular dipoles (Figure 3i). This increase of the work function facilitates the alignment of the energy band of NiO_x with the valance band energy of the perovskite films, thus improving the hole injection efficiency. In addition, the valence band edge of the NiO_x/SBTI film has an energy of 0.95 eV relative to the Fermi energy level, which is slightly higher than that of the NiO_x film (0.85 eV), thus facilitating the injection of holes from NiO_x into the per-

ovskite layer. The current density–voltage ($J-V$) characteristics of electron-only devices and hole-only devices were measured to quantify charge injection (Figure S15, Supporting Information). The electrons dominate charge injection in our devices, whereas the hole current is increased after the SBTI modification of the NiO_x, thus confirming beneficial effect of SBTI layer for achieving more balanced charge injection in NiO_x/SBTI based LEDs.

Enhanced optical properties of perovskite films based achieved with interfacial SBTI layer and the defect passivating 4-TMBABr are advantageous for PeLEDs devices. We produce PeLEDs with the following structures: ITO/NiO_x/SBTI/Perovskite/TPBi/LiF/Al (**Figure 4**a), which offers optimized energy band alignment for efficient charge injection (Figure 4b) and a set of control devices without the SBTI and/or 4-TMBABr. The EL peak of NiO_x/SBTI/4-TMBABr PeLEDs are centered at 487 nm (Figure 4c), which is consistent with the position of the PL peak, hence confirming that the EL signal is generated by the perovskites (inset in Figure 4c). The current injection is similar in all studies LEDs; however, improved luminance L and EQE in SBTI/4-TMBABr-based LED is observed due to decreased defect density of the perovskite film produced with 4-TMBABr (Figure 4d). The luminance observed for SBTI/4-TMBABr-based LEDs is up to 1094.9 cd m^{-2}, which is ≈2.5 times higher than that of the control LEDs (439.2 cd m^{-2}). Our studies of > 20 devices of each type revealed average EQE of 4.42% and 9.12% for control and SBTI/4-TMBABr-based LEDs, respectively, with the maximum EQE of 10.32% for SBTI/4-TMBABr based LEDs (Figure 4e,f and **Table 1**). With the

Table 1. Summary of the performance parameters of perovskite LEDs.

Devices	V_{on} [V]	EQE$_{max}$ [%]	L_{max} [cd m^{-2}]
NiO$_x$	3.5	4.39	439.2
NiO$_x$/SBTI	3.5	6.58	658.9
NiO$_x$/SBTI/4-TMBABr	3.0	10.32	1094.9

beneficial effects of the SBTI and 4-TMBABr, the resulting LEDs also shows a stable EL spectrum at different applied bias (Figure S16, Supporting Information), demonstrating the 4-TMBABr modified perovskite has better structural stability and with narrow full width at half maxima FWHM 23 nm, which enables an excellent color purity. In this device we observe Commission Internationale de L'Eclairage (CIE) chromaticity coordinate of (0.08, 0.28) (Figure S17, Supporting Information). More importantly, the SBTI/4-TMBABr exhibits a greatly improved half-lifetime with T_{50} = 52.3 min at an initial luminance of 100 cd m^{-2}, which is over 3-times longer than that of control LEDs (T_{50} = 16.7 min) (Figure S18, Supporting Information).

3. Conclusion

In summary, efficient PeLEDs with enhanced performance parameters and spectral stability are realized by 4-TMBABr passivation additive and SBTI interface modification layer. We demonstrated that 4-TMBABr additive can passivate or suppress the defect states at perovskites grain boundaries and at the interfaces due to the interaction of C=O function group and uncoordinated Pb^{2+} ions. The SBTI interface modification layer improves the perovskites film quality, reduces the potential barrier for the injecting hole and reduces the number of defect states at NiO$_x$ surface. In synergy, the treatment with 4-TMBABr and with SBTI enables us to realize PeLEDs with narrow blue emission, which is spectrally stable at operating voltages up to 8 V with maximum EQE up to 10.3% and increased half-lifetime of operation stability (52.3 min). Our strategy to produce high quality perovskite films is beneficial for LED applications, and could also offer advantages for applications in other optoelectronic devices.

4. Experimental Section

Preparation of NiO$_x$ Precursor Solution: NiO$_x$ precursor solution was prepared by mixing 0.25 mmol nickel acetate tetrahydrate and 15 µL ethanolamine in 5 mL ethanol, and the mixture was stirred at 60 °C for 6 h. The NiO$_x$ precursor solution was filtered with polytetrafluoroethylene filters (0.45 µm pore size) before use.

Synthesis of Precursor CsPbBr$_3$ Powder: PbBr$_2$ (20 mmol) and CsBr (20 mmol) were dissolved in 30 mL of 48% aqueous HBr solution and 10 mL of deionized water, respectively, followed by slow dropwise addition of aqueous CsBr solution to the PbBr$_2$ solution. The orange solid CsPbBr$_3$ was precipitated, followed by filtration to obtain CsPbBr$_3$ powder, which was washed five times with anhydrous ethanol and dried under vacuum for 30 min to obtain the dried CsPbB$_3$ powder.

Preparation of Quasi-2D Blue Perovskite Thin Film: PABr (0.15 mmol), PbBr$_2$ (0.015 mmol), PEABr (0.03 mmol), and CsPbBr$_3$ (0.15 mmol) were dissolved in 1 mL anhydrous DMSO to form the PEA$_x$PA$_{2-x}$(CsPbBr$_3$)$_{n-1}$PbBr$_4$ precursor solution. The mixture was stirred at 60 °C overnight and filtered with polytetrafluoroethylene filters (0.22 µm pore size) before use.

Fabrication of PeLEDs: The ITO-coated glass substrates (15 Ω sq^{-1}) were sonicated with detergent, deionized water, acetone, and isopropyl alcohol for 15 min each. The dried ITO substrates were treated with oxygen plasma for 15 min to improve the hydrophilicity and work function. The hole transport layer was prepared by spin-coating the NiO$_x$ precursor solution onto the ITO substrates (3000 rpm for 40 s) and annealed at 300 °C in the ambient conditions for 20 min. Subsequently, SBTI (0.12 wt.% in ethanol) layer was spin-coated (3000 rpm for 40 s) and annealed at 100 °C for 5 min. The substrates were transferred into a nitrogen glove box for device fabrication. The perovskite precursor solution was spin-coated (4000 rpm for 60 s), during the process 275 µL toluene was drop-cast onto the substrate at 25 s to promote the crystallization of perovskite, and then annealed at 80 °C for 10 min. TPBi (30 nm), LiF (1 nm), and Al (100 nm) layers were deposited by thermal evaporation under a pressure < 4 × 10^{-4} Pa in the vacuum chamber. The electron-only devices with structure of ITO/ZnO/perovskite/TPBI/LiF/Al and hole-only devices with ITO/NiO$_x$/SBTI/Perovskite(4-TMBABr)/MoO$_3$/Al configurations

Characterization of PeLEDs: The absorbance of perovskite films was acquired by Perkin Elmer Lambda 950 UV–vis-NIR spectrometer. PL steady-state, time-resolved spectra and PLQY data were measured on Edinburgh FLS920 PL spectrometer. XRD measurements were performed by an X-ray diffractometer (Bruker, D8 Advance) using Cu Kα (λ = 0.15 406 nm) as the X-ray source and scan angular range from 10° to 60° at a scanning rate of 6° min^{-1}. FE-SEM measurements were conducted on a JEOL JSM-7500F microscope. AFM images were collected with a Bruker Dimension Icon microscope in tapping mode. The contact angle measurements were performed using the OCA 15 EC system. XPS and UPS were analyzed by Thermo Scientific Escalab 250Xi. He I photons (21.2 eV) and the high-binding energy secondary electron cutoff (E_{cutoff}) were used to acquire the spectra at a normal emission level in UPS measurement, and the HOMO region data were calculated from the UPS spectra. The EL spectra characteristics of the PeLEDs were measured using a Shenzhen Pynect integrated sphere (50 cm in diameter) coupled with a Keithley 2400 sourcemeter. The operation lifetime tests of PeLEDs were conducted on a ZJZCL-1 OLED ageing lifespan test instrument. The grazing-incidence wide-angle X-ray scattering (GIWAXS) data were obtained at beamline BL14B1 of the Shanghai Synchrotron Radiation Facility (SSRF), China. A monochromatic beam of λ = 0.6887 Å was used, and the incident angle was 0.1°.

Supporting Information

Supporting Information is available from the Wiley Online Library or from the author.

Acknowledgements

Conflict of Interest

The authors declare no conflict of interest.

Data Availability Statement

The data that support the findings of this study are available from the corresponding author upon reasonable request.

[1] C. Zhang, S. Wang, X. Li, M. Yuan, L. Turyanska, X. Yang, *Adv. Funct. Mater.* **2020**, *30*, 1910582.

[2] H. Tsai, S. Shrestha, R. A. Vilá, W. Huang, C. Liu, C.-H. Hou, H.-H. Huang, X. Wen, M. Li, G. Wiederrecht, Y. Cui, M. Cotlet, X. Zhang, X. Ma, W. Nie, *Nat. Photonics* **2021**, *15*, 843.

[3] Q. A. Akkerman, G. Rainò, M. V. Kovalenko, L. Manna, *Nat. Mater.* **2018**, *17*, 394.

[4] Z.-K. Tan, R. S. Moghaddam, M. L. Lai, P. Docampo, R. Higler, F. Deschler, M. Price, A. Sadhanala, L. M. Pazos, D. Credgington, F. Hanusch, T. Bein, H. J. Snaith, R. H. Friend, *Nat. Nanotechnol.* **2014**, *9*, 687.

[5] M. Liu, Q. Wan, H. Wang, F. Carulli, X. Sun, W. Zheng, L. Kong, Q. Zhang, C. Zhang, Q. Zhang, S. Brovelli, L. Li, *Nat. Photonics* **2021**, *15*, 379.

[6] L. Kong, X. Zhang, Y. Li, H. Wang, Y. Jiang, S. Wang, M. You, C. Zhang, T. Zhang, S. V. Kershaw, W. Zheng, Y. Yang, Q. Lin, M. Yuan, A. L. Rogach, X. Yang, *Nat. Commun.* **2021**, *12*, 1246.

[7] Z. Liu, W. Qiu, X. Peng, G. Sun, X. Liu, D. Liu, Z. Li, F. He, C. Shen, Q. Gu, F. Ma, H.-L. Yip, L. Hou, Z. Qi, S.-J. Su, *Adv. Mater.* **2021**, *33*, 2103268.

[8] A. Fakharuddin, M. K. Gangishetty, M. Abdi-Jalebi, S.-H. Chin, A. R. bin Mohd Yusoff, D. N. Congreve, W. Tress, F. Deschler, M. Vasilopoulou, H. J. Bolink, *Nat. Electron.* **2022**, *5*, 203.

[9] Y. Gao, Y. Liu, F. Zhang, X. Bao, Z. Xu, X. Bai, M. Lu, Y. Wu, Z. Wu, Y. Zhang, Q. Wang, X. Gao, Y. Wang, Z. Shi, J. Hu, W. W. Yu, Y. Zhang, *Adv. Mater.* **2022**, *34*, 2207445.

[10] Q. A. Akkerman, T. P. T. Nguyen, S. C. Boehme, F. Montanarella, D. N. Dirin, P. Wechsler, F. Beiglbock, G. Raino, R. Erni, C. Katan, J. Even, M. V. Kovalenko, *Science* **2022**, *377*, 1406.

[11] S. Kumar, T. Marcato, F. Krumeich, Y. T. Li, Y. C. Chiu, C. J. Shih, *Nat. Commun.* **2022**, *13*, 2106.

[12] D. Yang, B. Zhao, T. Yang, R. Lai, D. Lan, R. H. Friend, D. Di, *Adv. Funct. Mater.* **2022**, *32*, 2109495.

[13] Y. Shen, Y.-Q. Li, K. Zhang, L.-J. Zhang, F.-M. Xie, L. Chen, X.-Y. Cai, Y. Lu, H. Ren, X. Gao, H. Xie, H. Mao, S. Kera, J.-X. Tang, *Adv. Funct. Mater.* **2022**, *32*, 2206574.

[14] W. Feng, Y. Zhao, K. Lin, J. Lu, Y. Liang, K. Liu, L. Xie, C. Tian, T. Lyu, Z. Wei, *Adv. Funct. Mater.* **2022**, *32*, 2203371.

[15] D. Ma, P. Todorović, S. Meshkat, M. I. Saidaminov, Y.-K. Wang, B. Chen, P. Li, B. Scheffel, R. Quintero-Bermudez, J. Z. Fan, Y. Dong, B. Sun, C. Xu, C. Zhou, Y. Hou, X. Li, Y. Kang, O. Voznyy, Z.-H. Lu, D. Ban, E. H. Sargent, *J. Am. Chem. Soc.* **2020**, *142*, 5126.

[16] Z. Chu, Y. Zhao, F. Ma, C.-X. Zhang, H. Deng, F. Gao, Q. Ye, J. Meng, Z. Yin, X. Zhang, J. You, *Nat. Commun.* **2020**, *11*, 4165.

[17] Z. Ren, L. Li, J. Yu, R. Ma, X. Xiao, R. Chen, K. Wang, X. W. Sun, W.-J. Yin, W. C. H. Choy, *ACS Energy Lett.* **2020**, *5*, 2569.

[18] F. Zhang, B. Cai, J. Song, B. Han, B. Zhang, H. Zeng, *Adv. Funct. Mater.* **2020**, *30*, 2001732.

[19] Q. Wang, X. Wang, Z. Yang, N. Zhou, Y. Deng, J. Zhao, X. Xiao, P. Rudd, A. Moran, Y. Yan, J. Huang, *Nat. Commun.* **2019**, *10*, 5633.

[20] N. Jiang, Z. Wang, Y. Zheng, Q. Guo, W. Niu, R. Zhang, F. Huang, D. Chen, *Nano Energy* **2022**, *97*, 107181.

[21] Y. Shen, K.-C. Shen, Y.-Q. Li, M. Guo, J. Wang, Y. Ye, F.-M. Xie, H. Ren, X. Gao, F. Song, J.-X. Tang, *Adv. Funct. Mater.* **2021**, *31*, 2006736.

[22] L. Kong, X. Zhang, C. Zhang, L. Wang, S. Wang, F. Cao, D. Zhao, A. L. Rogach, X. Yang, *Adv. Mater.* **2022**, *34*, 2205217.

[23] X. Zhang, D. Li, Z. Zhang, H. Liu, S. Wang, *Adv. Sci.* **2022**, *9*, 2200450.

[24] S. Liu, C. Zang, J. Zhang, S. Tian, Y. Wu, D. Shen, L. Zhang, W. Xie, C.-S. Lee, *Nano-Micro Lett.* **2021**, *14*, 14.

[25] W. Zheng, Q. Wan, Q. Zhang, M. Liu, C. Zhang, B. Wang, L. Kong, L. Li, *Nanoscale* **2020**, *12*, 8711.

[26] Y. Bai, H. Chen, S. Xiao, Q. Xue, T. Zhang, Z. Zhu, Q. Li, C. Hu, Y. Yang, Z. Hu, F. Huang, K. S. Wong, H.-L. Yip, S. Yang, *Adv. Funct. Mater.* **2016**, *26*, 2950.

[27] N. Li, S. Tao, Y. Chen, X. Niu, C. K. Onwudinanti, C. Hu, Z. Qiu, Z. Xu, G. Zheng, L. Wang, Y. Zhang, L. Li, H. Liu, Y. Lun, J. Hong, X. Wang, Y. Liu, H. Xie, Y. Gao, Y. Bai, S. Yang, G. Brocks, Q. Chen, H. Zhou, *Nat. Energy* **2019**, *4*, 408.

[28] S. Liu, Z. Guo, X. Wu, X. Liu, Z. Huang, L. Li, J. Zhang, H. Zhou, L.-D. Sun, C.-H. Yan, *Adv. Mater.* **2023**, *35*, 2208078.

[29] L. Zhang, F. Yuan, J. Xi, B. Jiao, H. Dong, J. Li, Z. Wu, *Adv. Funct. Mater.* **2020**, *30*, 2001834.

[30] H. Wang, X. Zhang, Q. Wu, F. Cao, D. Yang, Y. Shang, Z. Ning, W. Zhang, W. Zheng, Y. Yan, S. V. Kershaw, L. Zhang, A. L. Rogach, X. Yang, *Nat. Commun.* **2019**, *10*, 665.

[31] Y.-K. Wang, D. Ma, F. Yuan, K. Singh, J. M. Pina, A. Johnston, Y. Dong, C. Zhou, B. Chen, B. Sun, H. Ebe, J. Fan, M.-J. Sun, Y. Gao, Z.-H. Lu, O. Voznyy, L.-S. Liao, E. H. Sargent, *Nat. Commun.* **2020**, *11*, 3674.

[32] Z. Ren, J. Yu, Z. Qin, J. Wang, J. Sun, C. C. S. Chan, S. Ding, K. Wang, R. Chen, K. S. Wong, X. Lu, W. J. Yin, W. C. H. Choy, *Adv. Mater.* **2021**, *33*, 2005570.

[33] Y. Huang, Y. Li, E. L. Lim, T. Kong, Y. Zhang, J. Song, A. Hagfeldt, D. Bi, *J. Am. Chem. Soc.* **2021**, *143*, 3911.

[34] N. Li, Y. Jia, Y. Guo, N. Zhao, *Adv. Mater.* **2022**, *34*, 2108102.

[35] H. Yan, B. Wang, X. Yan, Q. Guan, H. Chen, Z. Shu, D. Wen, Y. Cai, *Mater. Today Energy* **2022**, *27*, 101038.

[36] Q. Liu, P. Lv, Y. Wang, Y. Zhu, M. Hu, F. Huang, Y.-B. Cheng, J. Lu, *Sol. RRL* **2022**, *6*, 2200232.

[37] X. Xu, H. Zhang, Y. Tong, Y. Sun, X. Fang, J. Xu, X. Wang, *Appl. Surf. Sci.* **2021**, *550*, 149316.

[38] M. Du, S. Zhao, L. Duan, Y. Cao, H. Wang, Y. Sun, L. Wang, X. Zhu, J. Feng, L. Liu, X. Jiang, Q. Dong, Y. Shi, K. Wang, S. Liu, *Joule* **2022**, *6*, 1931.